nuclear fusion
IAEA

PAPER • OPEN ACCESS

Heat pulse propagation and anomalous electron heat transport measurements on the optimized stellarator W7-X

To cite this article: G.M. Weir *et al* 2021 *Nucl. Fusion* **61** 056001

OPEN ACCESS
IOP Publishing | International Atomic Energy Agency Nuclear Fusion
Nucl. Fusion **61** (2021) 056001 (11pp) https://doi.org/10.1088/1741-4326/abea55

Heat pulse propagation and anomalous electron heat transport measurements on the optimized stellarator W7-X

G.M. Weir[1,*], P. Xanthopoulos[1], M. Hirsch[1], U. Höfel[1], T. Stange[1], N. Pablant[2], O. Grulke[1], S. Äkäslompolo[1], J. Alcusón[1], S. Bozhenkov[1], M. Beurskens[1], A. Dinklage[1], G. Fuchert[1], J. Geiger[1], M. Landreman[3], A. Langenberg[1], S. Lazerson[1], N. Marushchenko[1], E. Pasch[1], J. Schilling[1], E.R. Scott[1,4], Y. Turkin[1], T. Klinger[1] and the W7-X Team[a]

[1] Max-Planck-Institut für Plasmaphysik, 17491 Greifswald, Germany
[2] Princeton Plasma Physics Laboratory, Princeton, NJ 08536, United States of America
[3] University of Maryland, College Park, MD 20742, United States of America
[4] HSX Plasma Laboratory, University of Wisconsin-Madison, Madison, WI 53706, United States of America

E-mail: gavin.weir@ipp.mpg.de

Received 26 October 2020, revised 3 February 2021
Accepted for publication 26 February 2021
Published 26 March 2021

Abstract

The optimized stellarator Wendelstein 7-X (W7-X) is designed to have an approximately quasi-isodynamic magnetic configuration with reduced neoclassical transport in comparison to a classical stellarator, and turbulent transport is expected to be a significant source of anomalous heat transport across the plasma minor radius. The ion temperature gradient driven mode and the trapped electron mode (TEM) are thought to be responsible for the ion-scale turbulence in W7-X plasmas with volume averaged pressure below 1%. In this work, the electron temperature gradient driven turbulence is shown to be a good candidate for the explanation of the observed electron heat flux, in the inner plasma region where the density gradient is weak (in the outer region, a relatively stronger density gradient would drive additional TEM turbulence). The experimental electron heat transport measured during electron cyclotron resonant heating power and plasma density scans is compared to neoclassical predictions, and the stiffness in the electron heat transport measured during transient transport experiments is presented in three common magnetic configurations of W7-X. In low-$\langle\beta\rangle$ plasma discharges, the stiffness in the electron heat flux, quantified by the ratio of the heat pulse to power balance diffusivity, χ_e^{HP}/χ_e^{PB}, is measured to be less than 2, and trend downwards with increasing collisionality.

Keywords: stellarator, heat pulse, Wendelstein 7-X, drift waves, collisionality, ETG, TEM

(Some figures may appear in colour only in the online journal)

[*] Author to whom any correspondence should be addressed.
[a] See Klinger *et al* 2019 (https://doi.org/10.1088/1741-4326/ab03a7) for the W7-X Team.

1. Introduction

Turbulent processes are expected to dominate the electron energy and particle transport in magnetically confined fusion devices that are optimized to have low neoclassical transport. An important optimization criterion in the design of the Wendelstein 7-X (W7-X) device is to have reduced neoclassical transport through the reduction of the bounce-averaged radial drift of trapped electrons, while maintaining good magnetohydrodynamic (MHD) stability up to a volume averaged pressure of $\langle\beta\rangle \approx 5\%$. The neoclassical transport optimization of W7-X approximates a quasi-isodynamic magnetic configuration with a maximum in the second adiabatic invariant on its magnetic-axis (the so-called maximum-J property), and the level of quasi-isodynamicity is expected to improve with increasing plasma pressure in the optimized magnetic configurations of W7-X [1]. During the first high-performance operation phase of W7-X with an inertially cooled island divertor, the electron energy transport has been measured to be significantly larger than the neoclassical level in low-$\langle\beta\rangle$ discharges [2, 3] and a maximum $\langle\beta\rangle$ of 1.2% has been achieved [4].

In tokamak devices, which have low neoclassical transport, the electron temperature profile and its gradient has been measured to be resilient to changes in heating, and this effect has not been observed in classical stellarators [5]. Profile resiliency is the manifestation of stiffness in the electron heat flux, and gyrokinetic modeling indicates that stiffness in tokamak devices is driven by turbulent microinstabilities such as the electron temperature gradient (ETG) driven mode, the ion temperature gradient (ITG) driven mode and the trapped electron mode (TEM) (see, for instance, [6]). These instabilities are expected to be reduced in W7-X plasmas with sufficiently large pressure. In addition, similar to a tokamak, a sufficiently large pressure gradient in the W7-X stellarator would cause excitation of the kinetic ballooning mode [7], indicating that this instability may become relevant for future W7-X operation regimes, involving higher $\langle\beta\rangle$ values. In stark contrast, however, compared to a tokamak, the ETG driven turbulence is expected to be much more benign in the W7-X stellarator, thanks to the breaking of long streamers [8]. Notice that this feature by no means implies that the ETG transport is negligible, but merely lower compared to the ITG transport, assuming $T_e = T_i$, which is typically valid in the plasma periphery. In the core region, on the other hand, since electrons are hotter than ions, ETG turbulence is expected to be significant, as this work will demonstrate. We note that quasi-isodynamic magnetic configurations like W7-X are expected to be resilient to the (collisionless) TEM, due to the spatial separation between resonant trapping regions and regions of curvature drive [9, 10].

In this work, the electron heat transport driven by the electron temperature gradient is investigated in the core of W7-X using a combination of standard power balance transport analysis and heat pulse propagation measurements using modulated electron cyclotron resonant heating (ECRH). These measurements are used to assess the sensitivity of drift-wave driven turbulence to driving gradients in ECRH power deposition and plasma density scans during the first high-performance operation phase of W7-X. The stiffness in the electron heat flux, measured by the ratio of the heat pulse to power balance electron thermal diffusivity, χ_e^{HP}/χ_e^{PB}, is presented in three magnetic configurations of the W7-X stellarator: the 'high-mirror', the 'high-iota', and the 'standard' magnetic configurations of W7-X. The main differences between these three magnetic configurations, and the expected impact of these differences on ETG, ITG and TEM-driven electron heat transport are summarized in section 1.1. Matched profile experiments are presented in section 2 to assess the differences in anomalous electron heat flux between the three magnetic configurations, and the experimental anomalous electron thermal diffusivity is compared to expectations from ETG-mode driven electron heat transport. Heat pulse propagation measurements with varying electron collisionality are described in section 3 to assess the transition between TEM and ETG/ITG mode dominated electron heat transport, and the possible stabilization of TEM-driven turbulence with approximate quasi-isodynamicity.

1.1. Magnetic configuration effects in Wendelstein 7-X

The effective ripple (ϵ_{eff}), trapped particle fraction, and mean elongation are shown for the 'standard', 'high-mirror', and 'high-iota' magnetic configurations of W7-X in figure 1. The effective helical ripple is a dimensionless parameter that characterizes the effect of magnetic field geometry on neoclassical heat and particle transport in the $1/\nu$-regime [11]. The 'standard' configuration is expected to have the lowest level of neoclassical transport, while the 'high-mirror' configuration is expected to have the highest level of neoclassical transport. The 'high-iota' configuration is expected to have neoclassical transport that is intermediate to the other two. The trapped particle fraction in this case is an estimate of the ratio of electrons that are trapped in the magnetic field inhomogeneity in comparison to the total number of electrons. The trapped particle fraction is directly related to the number of particles available to contribute to TEM turbulence and is similar between all three magnetic configurations.

The mean elongation, approximated by $(\epsilon_t/b_{1,0})^2$ where ϵ_t is the inverse aspect ratio and $b_{1,0}$ represents the average toroidal curvature, directly modifies the neoclassical transport and also modifies the real-space gradients that drive turbulent transport. The mean elongation in W7-X is weakly correlated with the trapped particle fraction and highly correlated with rotational transform. The mean elongation in the 'high-iota' magnetic configuration is approximately 40% (60%) larger than that in the 'standard' ('high-mirror') magnetic configuration, suggesting that modes driven by gradients in the kinetic profiles should be exacerbated in the 'high-iota' magnetic configuration. Similarly to ITG modes, ETG instability responds to features of the local bad curvature and this curvature is similar among W7-X configurations that are currently available. The surface compression is an important mechanism that controls the electron temperature gradient in real space. This expectation is based on full-magnetic surface non-linear gyrokinetic calculations of ITG mode driven turbulence in magnetic configurations that are similar to those in W7-X [12]. These findings, however, are mostly applicable for the assumption of

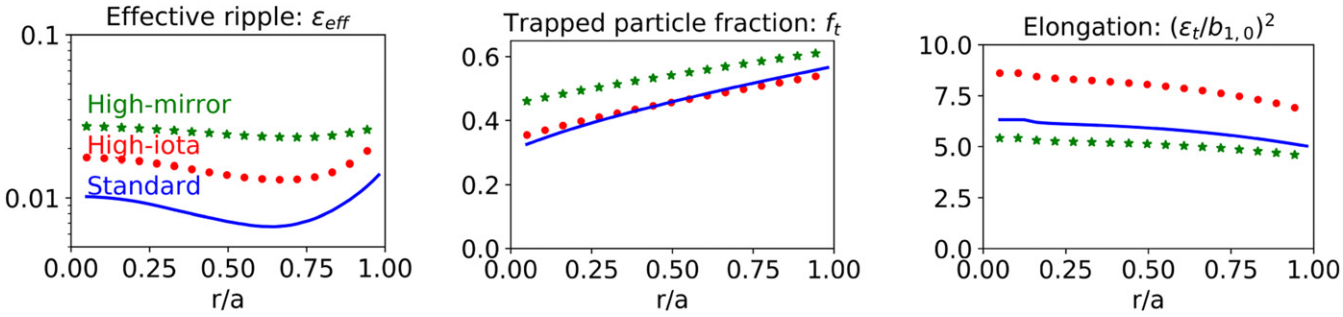

Figure 1. Radial profiles of the effective ripple, trapped particle fraction, and average elongation are shown for the 'high-mirror' (green stars), 'high-iota' (red circles), and 'standard' magnetic configurations (blue lines) of W7-X.

adiabatic electrons (i.e., ignoring electron trapping) which is not relevant for the estimation of the electron transport.

Reference [13] contains a detailed discussion of the theoretical impact of the maximum-J property on linear gyrokinetic calculations in these three magnetic configurations on W7-X. Specifically, figure 3(*e*) of reference [13] shows that deeply trapped particles near the half-radius of the 'high-mirror' and 'high-iota' magnetic configurations sample the maximum-J property, while deeply trapped particles sample less of this property in the 'standard' magnetic configuration. Consequently, assuming similar plasma parameters, the electron heat flux driven by TEM turbulence is expected to be larger in the 'standard' magnetic configuration than the 'high-mirror' or 'high-iota' magnetic configurations.

2. Matched profile experiments in three magnetic configurations

In order to compare the level of anomalous electron heat transport in each magnetic configuration, and to assess the impact of the magnetic configuration on the anomalous electron heat transport, it is necessary to match the kinetic profiles and their normalized gradients between configurations. The electron temperature profile in W7-X is measured using a combination of Thomson scattering [14, 15] and electron cyclotron emission (ECE) radiometry [16, 17] diagnostics. The line-average plasma density is measured by a single-channel interferometer [18], and the plasma density profile is measured through Thomson scattering. The ion temperature profile in W7-X is measured by an x-ray imaging crystal spectrometer (XICS) diagnostic [2, 19] and a charge exchange recombination spectroscopy (CXRS) diagnostic [20]. There is a small discrepancy between the ion temperature profiles measured by the XICS and CXRS diagnostics of approximately less than 200 eV; however, the XICS diagnostic was used exclusively for this work to avoid neutral beam injection heating.

The ion temperature profile is measured to be approximately equal to the electron temperature outside of 40%–60% of the plasma minor radius (r/a) and it is approximately flat within that radius. In the standard power balance analysis presented below, the ion temperature profile is taken to be equal to the electron temperature profile in regions where the ion temperature is measured to be greater than the electron temperature. The heating source for the ions in these discharges is collisional energy transfer from the electrons to the ions. Near the magnetic-axis the plasma species decouple due to the relatively high electron temperatures resulting in a small amount of collisional energy transfer between species. Generally, the collisional energy transfer varies between 30%–50% of the injected ECRH power in low-$\langle\beta\rangle$ W7-X discharges and is broadly distributed between 20%–50% of the plasma minor radius. The energy loss due to radiation is estimated by using an array of total power bolometers [21] to calculate the radiative emissivity in W7-X [22]. This measurement typically becomes non-negligible outside of $r/a > 0.7$ and leads to local flattening of the electron temperature profile, consequently the outer boundary for the transport analysis is limited to $r/a < 0.7$.

Table 1. A summary of parameters from the matched profile experiments.

W7-X program ID	Configuration	P_{ECRH} (MW)	W^{dia} (KJ)
XP:20180821.011	'Standard'	3.7	450 ± 10
XP:20180823.006	'High-mirror'	3.3	390 ± 10
XP:20180821.025	'Standard'	2.0	350 ± 10
XP:20180822.012	'High-iota'	1.7	320 ± 10

The experimental electron heat flux is determined by integrating the ECRH power deposition profile calculated using the TRAVIS ray tracing code [23], as

$$Q_{\mathrm{e}} = \langle q_{\mathrm{e}} \cdot \nabla\rho \rangle \frac{\mathrm{d}V}{\mathrm{d}\rho} = \int \frac{\mathrm{d}P}{\mathrm{d}V} \frac{\mathrm{d}V}{\mathrm{d}\rho} \mathrm{d}\rho, \qquad (1)$$

and subtracting the collisional energy exchange from the electrons to the ions from the ECRH flux, $Q_{\mathrm{e}} - Q_{\mathrm{e,i}}$. Here, the brackets $\langle\,\rangle$ represent flux-surface averaging, $\frac{\mathrm{d}V}{\mathrm{d}\rho}$ is the derivative of the enclosed plasma volume with respect to the normalized plasma minor radius (r/a), and $\frac{\mathrm{d}P}{\mathrm{d}V}$ is the net power deposition per unit enclosed plasma volume. The ambipolar neoclassical heat flux is calculated using the SFINCS code [24] from the kinetic profiles shown here. The magnetic equilibria used in this work were calculated using the variational moments equilibrium code [25]. The kinetic profile data was fit to a series of even-polynomial models using a weighted nonlinear least-squares fitting routine written in the python programming language that is based on the Levenberg–Marquard algorithm [26, 27]. The systematic uncertainties in the kinetic

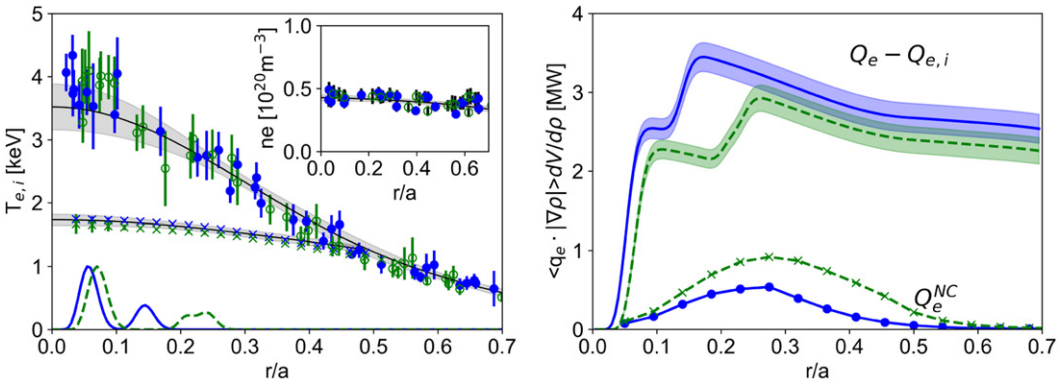

(a) Kinetic profile data (b) Electron heat flux

Figure 2. The electron (o) and ion temperature (x) profiles measured in the 'standard' (blue filled markers) and 'high-mirror' (green open markers) configurations are shown in (*a*) with plasma density profile measurements inset. The normalized ECRH power deposition profiles are also shown (lines). The electron flux from a power balance analysis (blue solid/green dashed lines) and the neoclassical result (blue-o/green-x) are shown for both configurations in (*b*).

profile data were propagated into the fits using a Monte-Carlo procedure that is described in reference [28].

The kinetic profiles were matched between the magnetic configurations by varying the ECRH power and deposition region [29] over multiple plasma discharges at a line-average plasma density of approximately 0.5×10^{20} m^{-3} and an on-axis magnetic field strength of $|B_o| = 2.52$ T. The total ECRH power, P_{ECRH}, and the diamagnetic stored energy, W^{dia} for each of the plasma discharges discussed in this section are shown in table 1.

The plasma density, electron temperature and ion temperature profiles measured in the 'standard' and 'high-mirror' magnetic configurations are shown in figure 2(*a*) for plasma discharge XP:20180821.011 and XP:20180823.006 respectively. The experimental electron heat fluxes from a power balance analysis are shown with the calculated neoclassical electron heat flux in figure 2(*b*).

Both discharges have a similar amount of heating power deposited within $r/a < 0.1$, but an additional 1.0 MW of off-axis heating power was required to match the kinetic profile shapes between discharges. The off-axis heating power was applied at $r/a \approx 0.2$ in the 'standard' configuration on discharge XP:20180821011 and at $r/a \approx 0.3$ in the 'high-mirror' configuration on discharge XP:20180823.006. The location of the off-axis heating is approximately coincident with the peak in the calculated neoclassical heat flux in each discharge. The anomalous component of the effective electron heat flux, the difference between the effective experimental heat flux and the neoclassical heat flux, is shown in figure 4(*a*). Since the kinetic profiles and their gradients are similar between the two discharges, we associate the difference in core anomalous electron heat transport with magnetic configuration effects on these discharges. The difference in anomalous electron heat flux between approximately $0.1 < r/a < 0.5$ is larger in the 'standard' configuration than in the 'high-mirror' configuration.

The plasma density, electron temperature and ion temperature profiles measured in the 'standard' and 'high-iota' magnetic configurations are shown in figure 3(*a*) for plasma discharge XP:20180821.025 and XP:20180822.012 respectively. The experimental and neoclassical electron heat fluxes for each discharge are shown in figure 3(*b*). The neoclassical electron heat transport in the 'standard'-3.7 MW case is larger than in the 'standard'-2.0 MW case between $0.1 < r/a < 0.4$, and this is primarily due to the difference in electron temperature (approximately 1 keV). No off-axis heating was necessary to match the kinetic profiles between the 'standard' and 'high-iota' magnetic configurations, with 2.0 and 1.7 MW of ECRH power deposited within $r/a < 0.1$ for each discharge respectively. The difference between the effective experimental and neoclassical electron heat flux is shown in figure 4 for each configuration, and it is higher in the 'standard' magnetic configuration across the plasma minor radius. We associate this difference with decreased turbulent electron heat transport in the 'high-iota' configuration in comparison to the 'standard' configuration.

In order to compare the anomalous electron heat transport between the three magnetic configurations, the effective power balance electron thermal diffusivity is calculated in flux-coordinates as in reference [30],

$$\chi_e^{PB} = -\langle q_e \cdot \nabla\rho\rangle / \left(n_e \langle |\nabla\rho|^2 \rangle \frac{\partial T_e}{\partial \rho} \right). \qquad (2)$$

Here n_e and T_e represent the electron plasma density and electron temperature respectively. The anomalous heat flux, shown in figure 4 is used in equation (2) to determine the anomalous electron thermal diffusivity, χ_e^{ANO}. The anomalous electron thermal diffusivities for each matched profile case is shown in figure 5. The electron thermal diffusivity cannot be determined accurately within $r/a < 0.15$ or outside of approximately $r/a > 0.65$ due to flattening of the electron temperature profile near the magnetic axis and near the edge and these regions are not shown in figure 5.

In the relatively higher heating power case that is shown in figure 5(*a*), χ_e^{ANO} is smaller in the 'high-mirror' configuration than the 'standard' configuration for $r/a < 0.5$ and χ_e^{ANO} is

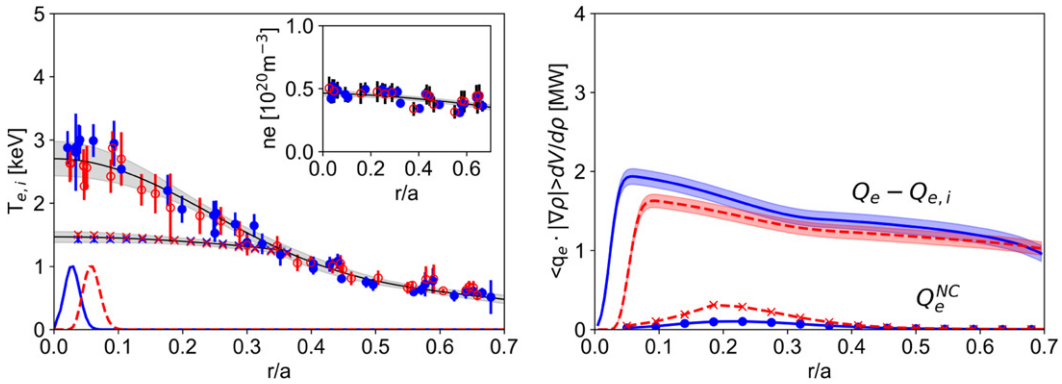

(a) Kinetic profile data (b) Electron heat flux

Figure 3. The electron (o) and ion temperature (x) profiles measured in the 'standard' (blue filled markers) and 'high-iota' (red open markers) configurations are shown in (*a*) with plasma density profile measurements inset. The normalized ECRH power deposition profiles are also shown (lines). The electron flux from a power balance analysis (blue solid/red dashed line) and the neoclassical result (blue-o/red-x) are shown for both configurations in (*b*).

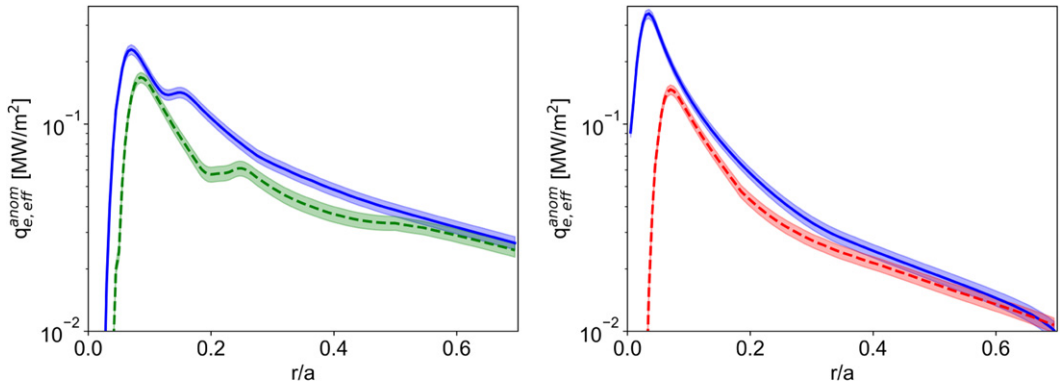

(a) "Standard" and "High-mirror" (b) "Standard" and "High-iota"

Figure 4. The effective anomalous electron heat flux for the 'standard' (solid blue), 'high-mirror' (dashed green), and 'high-iota' (dashed red) magnetic configurations for the corresponding matched profile experiments. The results from the 'standard' and 'high-mirror' configurations are shown in (*a*), and the results from the 'standard' and 'high-iota' configurations are shown in (*b*).

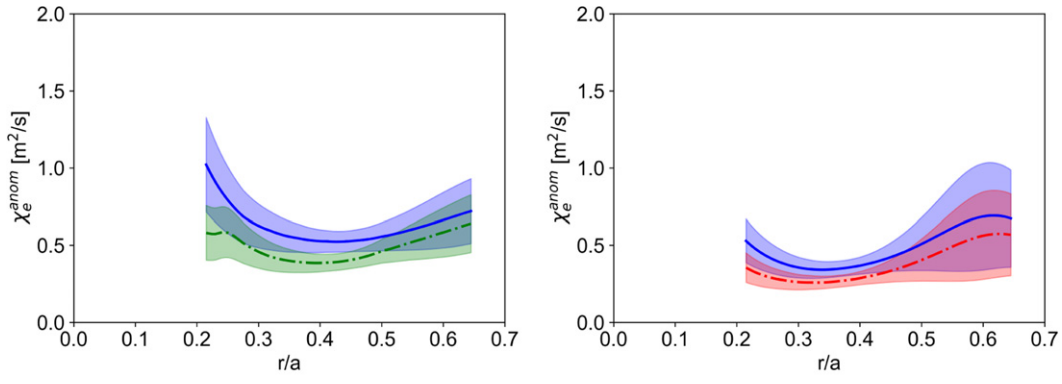

(a) "Standard" and "High-mirror" (b) "Standard" and "High-iota"

Figure 5. The anomalous electron thermal diffusivity, χ_e^{ANO}, for the 'standard' (solid blue), 'high-mirror' (dashed green), and 'high-iota' (dashed red) magnetic configurations for the corresponding matched profile experiments. The results from the 'standard' and 'high-mirror' configurations are shown in (*a*), and the results from the 'standard' and 'high-iota' configurations are shown in (*b*).

comparable outside of that radius. Similar behavior is observed in the relatively lower power case shown in figure 5(*b*), χ_e^{ANO} is smaller in the 'high-iota' configuration than the 'standard' configuration for $r/a < 0.5$, although the difference is smaller.

Table 2. Estimated electron thermal diffusivity resulting from ETG-driven turbulence at $r/a \approx 0.4$ for $a/L_{Te} = 3.6$, $a/L_{Ti} = 0$, and $a/L_{ne} = 0$ in the 'standard' magnetic configuration for two heating powers and varying $\tau = Z_{eff}T_e/T_i$ calculated from non-linear GENE simulations.

Configuration-P_{ech}	$\tau = Z_{eff}T_e/T_i$	1.0	1.5	2.0
'Standard'-3.7	χ_e^{ETG} (m^2 s^{-1})	0.7	0.5	0.4
'Standard'-2.0	χ_e^{ETG} (m^2 s^{-1})	0.35	0.25	0.2

The decreased anomalous electron heat flux in each case is consistent with reduced TEM activity in the core of W7-X due to increased approximate quasi-isodynamicity; however, it is also consistent with expectations from ETG driven electron heat transport in the core of W7-X.

In the region outside of $r/a > 0.45$ in the relatively higher power case and $r/a > 0.35$ in the relatively lower heating power case, $T_e \approx T_i$ and $a/L_{Te} \approx a/L_{Ti}$. Under those conditions the drives for electron- and ion-scale drift-wave turbulence are essentially equal, and the electron heat transport driven by TE and ITG modes is expected to dominate over that from ETG modes [8]. Inside of that region, $T_e > T_i$ and $a/L_{Te} > a/L_{Ti}$ hold, indicating that ETG driven electron heat transport can become important. Table 2 shows the electron thermal diffusivity in the 'standard' magnetic configuration from GENE [31, 32] nonlinear gyrokinetic simulations of the relatively higher heating power case. The normalized electron temperature gradient scale length in the relatively lower heating power case is approximately equal to that in the relatively higher heating power case at $r/a = 0.4$. The GENE simulations were performed with kinetic electrons, assuming an adiabatic ion response, in a collisionless, zero-pressure plasma ($\langle\beta\rangle = 0$) using a magnetic flux-tube geometry at $r/a = 0.4$. The inverse normalized scale lengths of the kinetic profile gradients were set equal to $a/L_{Te} = -a\mathrm{d}_r \ln(T_e) = 3.6$, $a/L_{Ti} = 0$, and $a/L_{ne} = 0$ in each case, and the parameter $\tau = Z_{eff}T_e/T_i$ was varied from 1.0 to 2.0, in accordance with the experimental conditions.

The experimental electron thermal diffusivities are in quantitative agreement with expectations from simulated ETG-driven electron heat transport in the 'standard' magnetic configuration in both heating power cases at $r/a = 0.4$. There is a small decrease in core anomalous electron thermal diffusivity measured in the 'high-iota' magnetic configuration over that measured in the 'standard' magnetic configuration, however the difference in the anomalous electron heat flux and the anomalous electron thermal diffusivity are similar between these configurations outside of approximately $r/a > 0.6$. These results are discussed further in the context of plasma collisionality scans in section 3.

3. Heat pulse propagation and stiffness measurements

Core plasma potential fluctuation measurements are not available from the first high-performance operation phase of W7-X, and we cannot yet determine an experimental turbulent electron heat flux from fluctuation measurements. For this reason, we have chosen to probe the sensitivity of the electron heat flux to the electron temperature gradient and collisionality using heat pulse propagation experiments and stiffness measurements.

During these experiments, a heat pulse modifies the local electron temperature gradient in the plasma and the spatiotemporal evolution of the electron temperature is used to solve a heat transport equation for the electron heat flux response (for example [33]). While the power balance electron thermal diffusivity quantifies the steady-state heat transport of an experiment, $\chi_e^{PB} = -q_e/n_e\nabla T_e$, the heat pulse diffusivity quantifies the local variation of the electron heat flux with temperature gradient, $\chi_e^{HP} = -\partial(q_e/n_e)/\partial\nabla T_e$, and is measured through perturbative transport experiments.

The ratio of the heat pulse to power balance electron thermal diffusivity, often referred to as the stiffness in the electron heat flux, is used to quantify profile resiliency. Where $\chi_e^{HP} \approx \chi_e^{PB}$ holds, the electron heat transport is diffusive. Where $\chi_e^{HP} > \chi_e^{PB}$ holds, the electron heat flux is primarily driven by the electron temperature gradient, and where $\chi_e^{HP} < \chi_e^{PB}$ holds, the electron heat flux is driven by another source (e.g., density gradient, driving TEM turbulence).

During the heat transport experiments described here, the power launched from a single gyrotron is modulated at 17 Hz at a duty cycle of 67% to enable heat pulse propagation measurements. A 17 Hz ECRH modulation is on the order of half the inverse energy confinement time in W7-X, estimated from the ratio of the diamagnetic stored energy to absorbed ECRH power (>95%), while a 67% duty cycle is beneficial for generating low frequency harmonics that can be used in the heat transport analysis. A modulation depth of less than 30% of the total launched power is sufficient to generate measurable heat pulses while maintaining a negligible density response at the modulation frequency.

The electron temperature response at the ECRH modulation frequency is measured through ECE radiometry. The logarithmic amplitude decay of the electron temperature perturbation and the cross-phase between the ECRH power and the electron temperature perturbation are used to determine the heat pulse diffusivity in flux-coordinates as in reference [30],

$$\chi_e^{HP} = -\frac{3}{4}\frac{\omega_{mod}}{\langle|\nabla\rho|^2\rangle}\left[\frac{\mathrm{d}\phi_\omega}{\mathrm{d}\rho}\left(\frac{\mathrm{d}\ \ln\ T_\omega}{\mathrm{d}\rho} + \frac{1}{2\rho} + \frac{1}{2}\frac{\mathrm{d}\ \ln\ n_e}{\mathrm{d}\rho}\right)\right]^{-1}. \quad (3)$$

Here the cyclic modulation frequency is ω_{mod}, and ϕ_ω and T_ω are the phase and amplitude of the electron temperature perturbation at the modulation frequency. This model is based on the reduced cylindrical model from reference [34], but it is generalized for analysis in flux-coordinates in order to facilitate comparisons with the effective power balance electron thermal diffusivity derived from equation (2). In this work, a minimum of ten modulation periods are used to determine the heat pulse amplitude and phase, and their respective derivatives were determined by linear fitting.

3.1. Heat pulse propagation in matched profile experiments

The heat pulse amplitude and phase-delay for the 'standard' -3.7 MW case (discharge XP:20180821.011) and the 'standard'-2.0 MW case (discharge XP:20180821.025) are

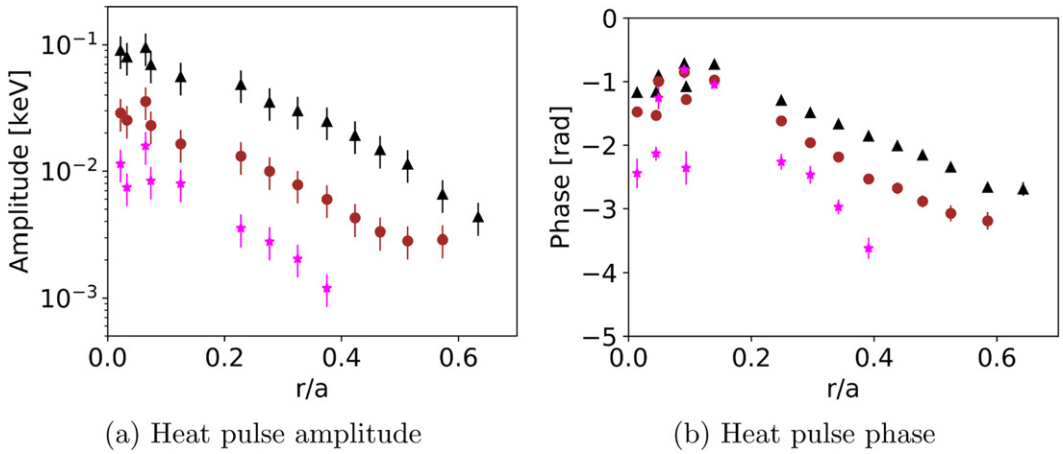

(a) Heat pulse amplitude (b) Heat pulse phase

Figure 6. Modulated electron temperature (*a*) amplitude and (*b*) phase response to modulated heating on discharge XP:20180821.011 ('standard'-3.7 MW). The electron temperature perturbation response for the first (black triangles), second (brown circles), and fourth (pink inverted triangles) modulation harmonics are shown for channels with coherence greater than 80%.

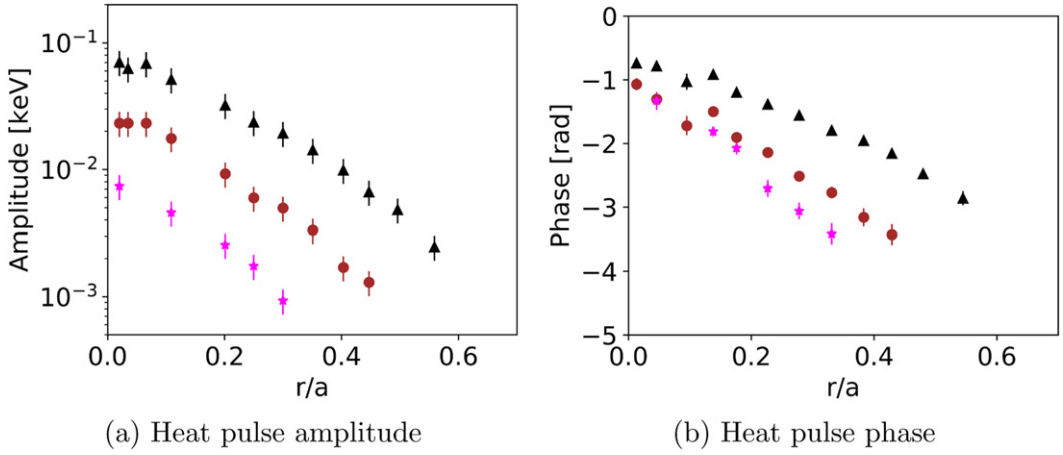

(a) Heat pulse amplitude (b) Heat pulse phase

Figure 7. Modulated electron temperature (*a*) amplitude and (*b*) phase response to modulated heating on discharge XP:20180821.025 ('standard'-2.0 MW). The electron temperature perturbation response for the first (black triangles), second (brown circles), and fourth (pink inverted triangles) modulation harmonics are shown for channels with coherence greater than 80%.

shown in figures 6 and 7 respectively for the first three modulation harmonics at 17, 34, and 68 Hz (referred to by their fundamental frequency multiplier as $n = 1$, 2, and 4 below).

The heat pulse amplitude shown in figures 6(*a*) and 7(*a*) decreases with the frequency of the harmonic as expected, $T_\omega \propto \omega_{\rm mod}^{-1}$ for the first three modulation harmonics and it is peaked in the region of ECRH deposition predicted by the TRAVIS ray tracing code. This effect is more clear in the heat pulse phase measurements that are shown in figures 6(*b*) and 7(*b*). In the 'standard'-3.7 MW case, the heat pulse phase is peaked near $r/a \approx 0.15$ corresponding with the off-axis heating source used on discharge XP:20180821.011. In the 'standard'-2.0 MW case, the heat pulse phase is peaked near the magnetic-axis corresponding to the on-axis heating source that was used on discharge XP:20180821.025. The heat pulse phase-delay and the logarithmic-amplitude decay decrease linearly outwards from the modulated ECRH source in both cases. The first harmonic of the ECRH modulation frequency has the highest signal-to-noise ratio and it is used for heat pulse propagation analysis throughout this work.

The heat pulse diffusivities measured during the matched profile experiments that are described in section 2 are shown in table 3. The normalized electron temperature scale length and the stiffness in the anomalous electron heat flux over the region of heat pulse propagation analysis is also included in table 3. The normalized density gradient scale length is approximately $a/L_{ne} = 0.3 \pm 0.2$ and the normalized ITG scale length is approximately $a/L_{Ti} = 1.1 \pm 0.4$ in all four cases.

The heat pulse diffusivities are comparable between the 'standard' configuration and the 'high-mirror' configuration at the relatively higher heating power. Similarly, the heat pulse diffusivities are comparable between the 'standard' configuration and the 'high-iota' configuration at relatively lower heating power. $\chi_e^{\rm HP}$ is approximately a factor of two larger in the 'standard'-3.7 MW case than in the 'standard'-2.0 MW case. The stiffness in the anomalous electron heat flux, $\chi_e^{\rm HP}/\chi_e^{\rm ANO}$ is also larger in the higher heating power case where larger

Table 3. Heat pulse propagation analysis results from the matched profile experiments. The effective collision frequency has been averaged over the region of heat pulse analysis $0.35 < r/a < 0.5$ and normalized by the effective ripple as in section 3.2.

Configuration-P_{ech}	ν^*_{eff}	χ_e^A ($m^2\ s^{-1}$)	χ_e^P ($m^2\ s^{-1}$)	χ_e^{HP} ($m^2\ s^{-1}$)	χ_e^{HP}/χ_e^{ANO}
'Standard'-3.7	0.02	0.5 ± 0.2	1.1 ± 0.1	0.7 ± 0.1	1.4 ± 0.2
'High-mirror'-3.3	0.04	0.4 ± 0.3	0.8 ± 0.1	0.6 ± 0.2	1.5 ± 0.2
'Standard'-2.0	0.06	0.2 ± 0.1	0.6 ± 0.1	0.4 ± 0.1	1.0 ± 0.1
'High-iota'-1.7	0.05	0.2 ± 0.1	0.6 ± 0.1	0.4 ± 0.1	1.3 ± 0.1

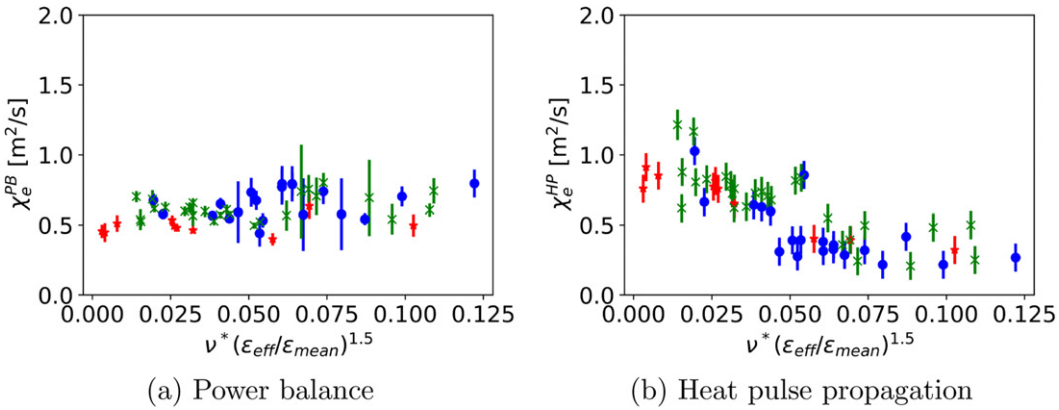

(a) Power balance (b) Heat pulse propagation

Figure 8. (*a*) The electron thermal diffusivity from a standard power balance analysis (*b*) and a heat pulse propagation analysis versus collisionality for the 'high-mirror' (green-x), 'high-iota' (red-∗), and the 'standard' (blue-o) magnetic configurations.

temperature gradients are achieved. The stiffness in the anomalous electron heat flux is greater than or equal to 1 in all four cases indicating increasing electron heat transport with ETG in W7-X. This result is consistent with ∇T-driven TEM and ETG driven electron heat transport in all four cases.

Nonlinear gyrokinetic calculations have previously been compared to power balance and profile resiliency measurements in the helically symmetric experiment (HSX), which is a stellarator optimised to have low neoclassical transport, where no profile resiliency was measured and the density gradient driven TEM was found to be the dominant turbulent transport mechanism across the majority of the plasma minor radius [30]. The neoclassical optimisation of HSX is expected to be particularly susceptible to TEM turbulence due to high correlation between trapping regions and curvature drive [35]. Conversely, the approximately quasi-isodynamic optimisation of the W7-X experiment is expected to lead to increased TEM stability.

3.2. Stiffness measurements in collisionality scans

While the TEM is stabilized by increasing collisionality due to collisional detrapping, the ETG/ITG modes are insensitive to collisions. In an attempt to identify the presence of and/or the possible stabilization of TEMs in W7-X, the collisionality was scanned by varying the launched ECRH power and line-average plasma density over multiple plasma discharges in the 'standard', 'high-mirror', and 'high-iota' magnetic configurations. This technique has previously been used to study the transition between TEM and ITG mode driven turbulence on the ASDEX Upgrade tokamak [36]. The reference collisionality used in this work is ν^* normalized by the bounce frequency of the trapped electrons,

$$\nu_{\rm eff} = \frac{\nu^*}{\omega_{\rm B}} = 2\pi a_{\rm p} \frac{\nu_{\rm e,i}/\epsilon_{\rm eff}}{f_{\rm tr}(c_{\rm s}/a)\iota r_{\rm eff}},$$

where $\nu_{\rm e,i}$ is the electron–ion collision frequency, $\iota/2\pi$ is the rotational transform, $c_{\rm s}$ is the ion-acoustic velocity, $r_{\rm eff}$ is the effective plasma minor radius, and a is the plasma minor radius. The collisionality is dependent on the electron and ion temperature and the plasma density, and variations in the collisionality are correlated with variations in these parameters and their gradients. The power balance and heat pulse electron thermal diffusivities are shown versus collisionality for all three magnetic configurations in figures 8(*a*) and (*b*) respectively. Following reference [36] the collisionality in figure 8 and in figure 9 is scaled by $(\epsilon_{\rm eff}/\epsilon_{\rm mean})^{1.5}$ where $\epsilon_{\rm mean}$ is the average effective ripple of the three magnetic configurations. Note that the trapped particle fraction is often approximated by $f_{\rm tr} \approx \sqrt{\epsilon_{\rm eff}}$, and this normalization removes some of the differences in collisionality between magnetic configurations.

The average χ_e^{PB} over the region of heat pulse propagation analysis does not vary significantly with collisionality in figure 8(*a*), while the heat pulse diffusivity varies by a factor of approximately four from the lowest collisionalities to the highest collisionalities in figure 8(*b*). The resulting stiffness in the electron heat flux, shown in figure 9(*a*), trends downwards with increasing collisionality between approximately 2 and 0.5 for the data shown in figure 8. The power balance electron thermal diffusivity is less sensitive to changes in transport than the heat pulse electron thermal diffusivity, and the majority of this

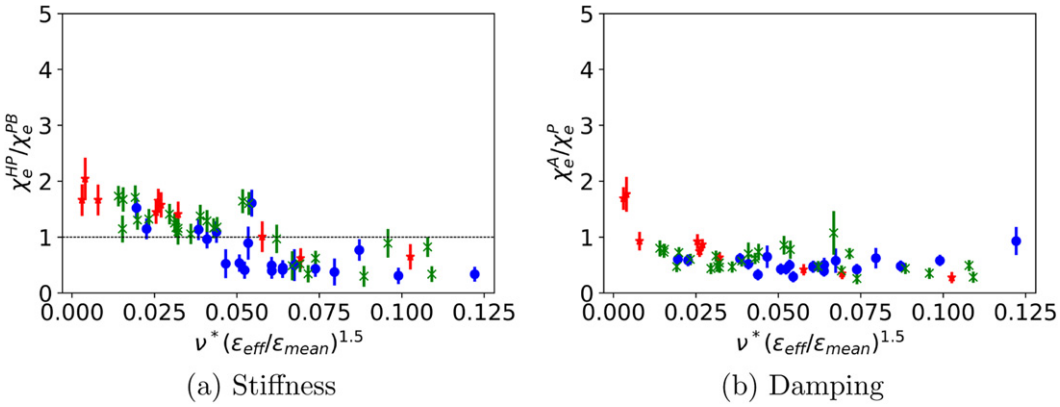

Figure 9. (*a*) The stiffness in the electron heat flux and (*b*) the ratio of the heat pulse diffusivity from the amplitude and that from the phase versus collisionality for the 'high-mirror' (green-x), 'high-iota' (red-*), and the 'standard' (blue-o) magnetic configurations.

variation in stiffness is due to variation in χ_e^{HP}. A stiffness in the electron heat flux of less than 2 is comparable to measurements in other stellarator experiments and is less than that measured in tokamak experiments with profile resiliency [5, 30].

During evaluation of the heat pulse diffusivity it is common to separate the contributions from the phase and amplitude into two independent measurements to better understand the underlying heat transport. The ratio of the diffusivity from the amplitude and the diffusivity from the phase can indicate whether the perturbation propagates diffusively or convectively with higher sensitivity than the stiffness in the electron heat flux. This is easiest to understand by modeling the heat pulse propagation as a damped plane-wave in a slab geometry, $T_\omega \propto \mathrm{e}^{-\alpha x}\,\mathrm{e}^{\mathrm{i}(kx-\omega t)}$. The wave-vector is $k = \mathrm{d}\varphi/\mathrm{d}x$ and the spatial damping rate is $\alpha = \Re(-\mathrm{d}\,\ln\,T_\omega/\mathrm{d}x)$. Then the ratio of the diffusivity from the amplitude and the diffusivity from the phase is

$$\frac{\chi_\mathrm{e}^\mathrm{A}}{\chi_\mathrm{e}^\mathrm{P}} = \frac{(\mathrm{d}\varphi/\mathrm{d}x)^2}{(\mathrm{d}\,\ln\,T_\omega/\mathrm{d}x)^2} = \frac{(\omega/\alpha)^2}{v_\varphi^2},$$

where v_φ is the phase-velocity of the heat pulse. In the slab model, if $\chi_\mathrm{e}^\mathrm{A}/\chi_\mathrm{e}^\mathrm{P} > 1$ the length-scale required for the perturbation to damp is longer than the characteristic distance that the perturbation travels during one wave-period (the perturbation moves convectively). If $\chi_\mathrm{e}^\mathrm{A}/\chi_\mathrm{e}^\mathrm{P} < 1$, the perturbation damps away faster than it propagates during one wave-period, and if $\chi_\mathrm{e}^\mathrm{A}/\chi_\mathrm{e}^\mathrm{P} \approx 1$, then the perturbation damps over approximately the same distance that it propagates during one wave-period.

Due to effective damping terms in the cylindrical heat equation, $\chi_\mathrm{e}^\mathrm{A} \leqslant \chi_\mathrm{e}^\mathrm{P}$ under normal diffusive conditions [34]. $\chi_\mathrm{e}^\mathrm{A} > \chi_\mathrm{e}^\mathrm{P}$ occurs under convective conditions, such as those that occur in tokamak devices above a critical electron temperature gradient. This effect has been successfully modeled using linear gyrokinetic simulations of the TEM and an empirical model for heat pulse propagation on the ASDEX Upgrade tokamak [36]. $\chi_\mathrm{e}^\mathrm{A} > \chi_\mathrm{e}^\mathrm{P}$ can indicate that heat pulses are moving in the same direction as a convective flow and $\chi_\mathrm{e}^\mathrm{A} < \chi_\mathrm{e}^\mathrm{P}$ can indicate the opposite [37]. The data in figure 9(*b*) indicates that the direction of the convective heat velocity appears to change sign to be in the same direction as the heat pulse propagation at the lowest collisionalities; however, the magnitude of the convective heat transport component cannot be determined from the data presented in figures 9(*a*) and (*b*) and requires further study.

In the region of heat pulse propagation analysis on W7-X, linear gyrokinetic calculations indicate that the 'high-iota' and 'high-mirror' magnetic configurations are more stable against TEMs than the 'standard' magnetic configuration [13]. $\chi_\mathrm{e}^\mathrm{A} \leqslant \chi_\mathrm{e}^\mathrm{P}$ in the 'standard' magnetic configuration and in all three magnetic configurations at relatively higher collisionalities. In the 'high-iota' magnetic configurations $\chi_\mathrm{e}^\mathrm{A} > \chi_\mathrm{e}^\mathrm{P}$ at the lowest collisionalities shown in figure 9(*b*). The change in heat pulse electron thermal diffusivity with collisionality can represent either a decrease in TEM activity by collisional detrapping or an increase in ETG mode activity due to increased ETG drive at low-collisionality.

4. Summary and conclusions

The electron heat transport in the W7-X stellarator has been studied using a combination of steady-state and perturbative transport experiments in three magnetic configurations during the first high-performance operational phase of the device with an inertially cooled divertor. The electron thermal diffusivity and the stiffness in the electron heat flux have been measured in matched profile experiments and in collisionality-scans in all three magnetic configurations. Although the 'standard' magnetic configuration of W7-X has the lowest level of neoclassical electron heat transport, the anomalous component of the electron heat transport is measured to be higher in the 'standard' magnetic configuration than in either the 'high-mirror' or 'high-iota' magnetic configurations during matched profile experiments. The primary difference in electron heat transport is measured within $r/a < 0.4$ where the anomalous electron thermal diffusivity is higher in the 'standard' magnetic configuration than in the other two.

For $r/a < 0.4$, the electron temperature and its normalized inverse scale length are larger than the ion temperature and its normalized inverse scale length indicating that the drive for electron-scale turbulence is larger than the drive for ion-scale

turbulence. The electron thermal diffusivity resulting from ETG-driven turbulence at $r/a = 0.4$, modeled by non-linear gyrokinetic simulations with adiabatic ions, is in quantitative agreement with the anomalous electron thermal diffusivity measured in the 'standard' magnetic configuration at that location. For $r/a > 0.4$, the drive for electron- and ion-scale turbulence are approximately equal, and TE/ITG mode driven turbulence is expected to dominate.

The 'high-mirror' and 'high-iota' magnetic configurations have a higher degree of approximate quasi-isodynamicity (maximum-J) than the 'standard' magnetic configuration within $r/a < 0.5$, and the anomalous electron heat transport in that region is measured to be reduced in these magnetic configurations during matched profile experiments. The stiffness in the anomalous electron heat flux is measured to be greater than or equal to 1 in all four cases, which is consistent with ∇T-driven TEM and ETG mode turbulence.

During ECRH power and collisionality scans the stiffness in the electron heat flux, χ_e^{HP}/χ_e^{PB}, is measured to trend downwards with collisionality between approximately 2.0 and 0.5 in all three magnetic configurations. This is consistent with collisional stabilization of TEMs, but it is also consistent with a possible transition to ITG mode driven electron turbulence. The change in χ_e^{HP}/χ_e^{PB} is primarily due to a decrease in χ_e^{HP} with increasing collisionality. At relatively higher collisionalities, the perturbative diffusivity measured using the amplitude decay of heat pulses, χ_e^{A}, is smaller than that measured using the phase delay of heat pulses, χ_e^{P}. This is consistent with diffusive electron heat transport at the relatively higher collisionalities. At relatively lower-collisionalities, χ_e^{A}/χ_e^{P} trends upwards in the 'high-iota' magnetic configuration of W7-X indicating a transition to convective electron heat transport.

Acknowledgments

This work has been carried out within the framework of the EUROfusion Consortium and has received funding from the Euratom research and training program 2014–2018 and 2019–2020 under Grant Agreement No. 633053. The views and opinions expressed herein do not necessarily reflect those of the European Commission.

Appendix. Variation with ECRH modulation frequency

The purpose of heat pulse propagation experiments is to assess the linearity of the electron heat flux with respect to the electron temperature gradient. Generally it is possible to separate and measure the convective and diffusive components of that heat flux using the variation of the heat pulse diffusivity with ECRH modulation frequency as is proposed in reference [34].

The heat pulse diffusivities for the first three ECRH modulation harmonics in the region between $0.2 < r/a < 0.4$ are shown in figure A1 for discharge XP:20180821.011 ('standard'-3.7 MW). There is no significant variation with frequency indicating that the transport is primarily diffusive in this case. In the experiments presented in this work, the harmonics of the ECRH modulation frequency have low signal-to-noise ratio in the region of interest, $0.35 < r/a < 0.5$, and we have chosen to use the ratio of the diffusivity from the heat pulse amplitude and phase to indicate the presence of convection because this information is also available in the fundamental harmonic content.

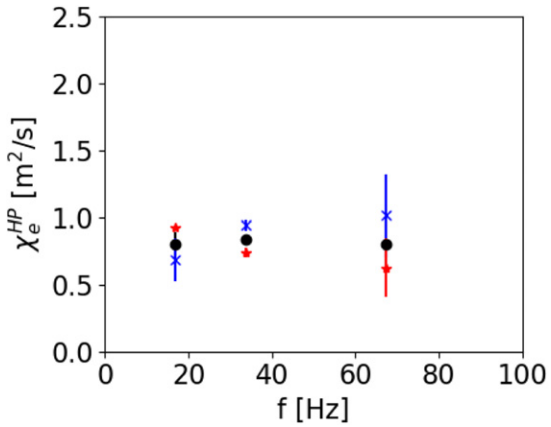

Figure A1. The heat pulse diffusivity from the amplitude decay (blue-x), phase delay (red-∗) and their geometric mean (black-o) versus ECRH modulation frequency harmonic in the region between $0.2 < r/a < 0.4$ for discharge XP:20180821.011 ('standard'-3.7 MW).

ORCID iDs

G.M. Weir https://orcid.org/0000-0002-2370-409X
N. Pablant https://orcid.org/0000-0001-6617-8459
J. Alcusón https://orcid.org/0000-0001-5492-7432
S. Bozhenkov https://orcid.org/0000-0003-4289-3532
J. Geiger https://orcid.org/0000-0003-4268-7480
A. Langenberg https://orcid.org/0000-0002-2107-5488
S. Lazerson https://orcid.org/0000-0001-8002-0121
J. Schilling https://orcid.org/0000-0002-6363-6554

References

[1] Nührenberg J. and Zille R. 1986 Stable stellarators with medium β and aspect ratio *Phys. Lett.* A **114** 129–32
[2] Pablant N.A. *et al* 2018 Core radial electric field and transport in Wendelstein 7-X plasmas *Phys. Plasmas* **25** 022508
[3] Dinklage A. *et al* 2018 Magnetic configuration effects on the Wendelstein 7-X stellarator *Nat. Phys.* **14** 855–60
[4] Klinger T. *et al* 2019 Overview of first Wendelstein 7-X high-performance operation *Nucl. Fusion* **59** 112004
[5] Stroth U. 1998 A comparative study of transport in stellarators and tokamaks *Plasma Phys. Control. Fusion* **40** 9
[6] Ryter F. *et al* 2006 Electron heat transport studies *Plasma Phys. Control. Fusion* **48** B453–63
[7] Aleynikova K., Zocco A., Xanthopoulos P., Helander P. and Nührenberg C. 2018 Kinetic ballooning modes in tokamaks and stellarators *J. Plasma Phys.* **84** 745840602
[8] Plunk G.G. *et al* 2019 Stellarators resist turbulent transport on the electron Larmor scale *Phys. Rev. Lett.* **122** 035002
[9] Proll J.H.E., Helander P., Connor J.W. and Plunk G.G. 2012 Resilience of quasi-isodynamic stellarators against trapped-particle instabilities *Phys. Rev. Lett.* **108** 245002

[10] Plunk G.G., Connor J.W. and Helander P. 2017 Collisionless microinstabilities in stellarators. Part 4. The ion-driven trapped-electron mode *J. Plasma Phys.* **83** 715830404
[11] Nemov V.V., Kasilov S.V., Kernbichler W. and Heyn M.F. 1999 Evaluation of $1/\nu$ neoclassical transport in stellarators *Phys. Plasmas* **6** 4622–32
[12] Xanthopoulos P. *et al* 2014 Controlling turbulence in present and future stellarators *Phys. Rev. Lett.* **113** 155001
[13] Alcuson J.A., Xanthopoulos P., Plunk G.G., Helander P., Wilms F., Turkin Y., von Stechow A. and Grulke O. 2019 Suppression of electrostatic micro-instabilities in maximum-J stellarators *Plasma Phys. Control. Fusion* **62** 035005
[14] Pasch E., Beurskens M.N.A., Bozhenkov S.A., Fuchert G., Knauer J. and Wolf R.C. 2016 The Thomson scattering system at Wendelstein 7-X *Rev. Sci. Instrum.* **87** 11E729
[15] Bozhenkov S.A. *et al* 2017 The Thomson scattering diagnostic at Wendelstein 7-X and its performance in the first operation phase *J. Inst.* **12** P10004
[16] Hirsch M. *et al* 2019 ECE diagnostic for the initial operation of Wendelstein 7-X *EPJ Web Conf.* **203** 03007
[17] Hoefel U. *et al* 2019 Bayesian modeling of microwave radiometer calibration on the example of the Wendelstein 7-X electron cyclotron emission diagnostic *Rev. Sci. Instrum.* **90** 043502
[18] Brunner K.J. *et al* 2018 Real-time dispersion interferometry for density feedback in fusion devices *J. Inst.* **13** P09002
[19] Kring J. *et al* 2018 *In situ* wavelength calibration system for the x-ray imaging crystal spectrometer (XICS) on W7-X *Rev. Sci. Instrum.* **89** 10F107
[20] Ford O.P. *et al* 2020 Charge exchange recombination spectroscopy at Wendelstein 7-X *Rev. Sci. Instrum.* **91** 023507
[21] Zhang D. *et al* 2010 Design criteria of the bolometer diagnostic for steady-state operation of the W7-X stellarator *Rev. Sci. Instrum.* **81** 10E134
[22] Zhang D. *et al* 2019 First observation of a stable highly dissipative divertor plasma regime on the Wendelstein 7-X stellarator *Phys. Rev. Lett.* **123** 025002
[23] Marushchenko N.B., Turkin Y. and Maassberg H. 2014 Ray-tracing code TRAVIS for ECR heating, EC current drive and ECE diagnostic *Comput. Phys. Commun.* **185** 165–76
[24] Landreman M., Smith H.M., Mollén A. and Helander P. 2014 Comparison of particle trajectories and collision operators for collisional transport in nonaxisymmetric plasmas *Phys. Plasmas* **21** 042503
[25] Hirshman S.P. and Whitson J.C. 1983 Steepest-descent moment method for three-dimensional magnetohydrodynamic equilibria *Phys. Fluids* **26** 3553–68
[26] Moré J.J. 1978 The Levenberg–Marquardt algorithm: implementation and theory *Numerical Analysis* (*Lecture Notes in Mathematics*) ed G.A. Watson (Berlin: Springer) pp 105–16
[27] Markwardt C.B. 2009 Non-linear least-squares fitting in IDL with MPFIT *ADASS XVIII Conference 2-5 November, 2008 Quebec City, Quebec, Canada* D. Bohlender, D. Durand and P. Dowler (*ASP Conf. Ser.* vol 411) p 251 (arXiv:0902.2850)
[28] Weir G.M. 2014 Heat transport experiments on the HSX stellarator *PhD Thesis* The University of Wisconsin-Madison, Wisconsin, United States
[29] Wolf R.C. *et al* 2018 Electron-cyclotron-resonance heating in Wendelstein 7-X: a versatile heating and current-drive method and a tool for in-depth physics studies *Plasma Phys. Control. Fusion* **61** 014037
[30] Weir G.M., Faber B.J., Likin K.M., Talmadge J.N., Anderson D.T. and Anderson F.S.B. 2015 Profile stiffness measurements in the helically symmetric experiment and comparison to nonlinear gyrokinetic calculations *Phys. Plasmas* **22** 056107
[31] Jenko F., Dorland W., Kotschenreuther M. and Rogers B.N. 2000 Electron temperature gradient driven turbulence *Phys. Plasmas* **7** 1904
[32] Xanthopoulos P., Cooper W.A., Jenko F., Turkin Y., Runov A. and Geiger J. 2009 A geometry interface for gyrokinetic microturbulence investigations in toroidal configurations *Phys. Plasmas* **16** 082303
[33] Ryter F. *et al* 2001 Experimental studies of electron transport *Plasma Phys. Control. Fusion* **43** A323
[34] Jacchia A., Mantica P., De Luca F. and Gorini G. 1991 Determination of diffusive and nondiffusive transport in modulation experiments in plasmas *Phys. Fluids* B **3** 3033–40
[35] Faber B.J., Pueschel M.J., Proll J.H.E., Xanthopoulos P., Terry P.W., Hegna C.C., Weir G.M., Likin K.M. and Talmadge J.N. 2015 Gyrokinetic studies of trapped electron mode turbulence in the helically symmetric experiment stellarator *Phys. Plasmas* **22** 072305
[36] Ryter F., Angioni C., Peeters A.G., Leuterer F., Fahrbach H.U. and Suttrop W. 2005 Experimental study of trapped-electron-mode properties in tokamaks: threshold and stabilization by collisions *Phys. Rev. Lett.* **95** 085001
[37] Luce T.C., DeBoo J.C., Howard N., Liu C. and Petty C.C. 2005 Search for threshold behavior in DIII-D electron heat transport *Proc. 32nd EPS Conf. on Plasma Phys. ECA* (*27 June, 2005 Tarragona, Spain*) vol 29C p P5.038